Highlights

Subduction-driven mantle flow beneath and around the Philippine Sea Plate from seismic anisotropy

- New technique enables us to infer shear-wave splitting near the Philippine Sea Plate.
- Widespread trench-parallel fast directions, and toroidal flow around slab edges.
- Inferred mantle flow beneath the Philippine Plate differs from absolute plate motion.
- Flow is driven by nearby subduction, in agreement with geodynamic models.

Subduction-driven mantle flow beneath and around the Philippine Sea Plate from seismic anisotropy

Jonathan Wolf[1,2,3,*], Frederik Link[4], Maureen D. Long[4], Edward Garnero[5], John D. West[5]

Abstract

Shear-wave splitting illuminates mantle flow and subduction zone dynamics but is typically inferred near stations or earthquakes, limiting studies in sparsely instrumented regions away from earthquakes. Where stations or earthquakes are present, fast splitting directions are often parallel to the nearest trench, which has yet to be fully understood and reconciled with geodynamic flow predictions. Here we use a novel technique that leverages surface-reflected PS and PPS waves to overcome limitations in coverage beneath the Philippine Sea Plate, which is surrounded on all sides by subducting slabs. Upper mantle deformation in this region, best explained by mantle flow below 250 km depth, is generally different from the absolute plate motion direction and instead shaped by the surrounding subduction zones. We interpret our observations as likely evidence for trench-parallel flow in the mantle wedge beneath the Ryukyu, Nankai, and parts of the Izu-Bonin subduction zones, as well as toroidal flow around the Ryukyu and Mariana slab edges. Beneath the Pacific Plate, near the Mariana subduction zone, flow is trench-perpendicular. Our results are generally consistent with flow patterns predicted by previous geodynamic models, and provide a new constraint on subduction-driven deformation in the region.

*Corresponding author
Email address: wolf@ucsc.edu (Jonathan Wolf)
[1]Department of Earth and Planetary Sciences, University of California, Santa Cruz, CA, USA
[2]Department of Earth and Planetary Science, University of California, Berkeley, CA, USA
[3]Miller Institute for Basic Research in Science, Berkeley, CA, USA
[4]Department of Earth and Planetary Sciences, Yale University, New Haven, CT, USA
[5]School of Earth and Space Exploration, Arizona State University, Tempe, AZ, USA

Keywords: Philippine Sea Plate, Seismic anisotropy, Shear-wave splitting, Upper mantle, Slab-driven flow, PS splitting

1. Introduction

The Philippine Sea Plate is bounded by multiple subduction systems, including the Ryukyu, Izu–Bonin–Mariana, and Philippine trenches (Figure 1c). These subduction systems have varying slab geometries and trench migration velocities (e.g., Heuret and Lallemand, 2005; Hayes et al., 2018; Fukao and Obayashi, 2013), making the region uniquely suitable for investigating the deformation and flow of the mantle in response to subduction. Flow and deformation can cause the preferential alignment of individual mineral crystals (e.g., Karato et al., 2008; Long and Becker, 2010), leading to variations in seismic wave speeds that depend on propagation direction and/or polarization (that is, seismic anisotropy). Therefore, the anisotropic structure of the upper mantle across the Philippine Sea Plate can shed light on the dynamics of plate–mantle coupling, the geometry of subduction-driven flow, and the mechanical interactions between slabs and the surrounding mantle (e.g., Song and Kawakatsu, 2012; Long, 2013; Faccenda, 2014).

Seismic station coverage near the Philippine Sea Plate is sparse. Studies that use surface waves and body wave travel times (e.g., Fan and Zhao, 2019; Isse et al., 2010; Fan et al., 2024) have been conducted, capturing large-scale upper mantle flow patterns in the region; however, they lack the lateral resolution of body waves for resolving smaller-scale slab-mantle interactions. Constraints from shear-wave splitting measurements, which detect the birefringence of seismic shear waves after they have traveled through anisotropic mantle material, are often used to achieve a detailed, laterally resolved view of flow in Earth's upper mantle; however, due to the limited station coverage, mantle deformation and flow have only been studied using shear wave splitting measurements at a few locations within this region (e.g., Pozgay et al., 2007; Wirth and Long, 2010; Yeh et al., 2013; Wang and He, 2020). To overcome this limitation, we build on an approach based on surface-reflected seismic phases. This shear-wave splitting technique was first introduced by Su and Park (1994) and applied to PS waves (Figure 1a), and later refined and validated by Wolf and Long (2023). To enhance raypath coverage, we extend this method to PPS waves, enabling us to infer seismic anisotropy beneath the PS and PPS P-to-SV conversion regions.

Shear-wave splitting measurements are typically attributed to upper mantle anisotropy that results from deformation, primarily due to aligned olivine. Olivine can develop different crys-

tallographic fabrics, meaning that the preferred orientation of its crystal axes varies depending on temperature, stress, and water content in the mantle (e.g., Karato et al., 2008). These fabrics control how seismic waves propagate and thus the orientation of seismic anisotropy. For typical A-, C-, or E-type olivine fabrics, each defined by different dominant slip systems, the fast polarization direction of vertically incident shear waves generally aligns with the direction of shear in the upper mantle, in regions dominated by horizontal deformation (e.g., Karato et al., 2008). As a result, the fast polarization azimuth of seismic anisotropy is generally parallel to mantle flow, as in regions of horizontal shear with a vertical velocity gradient. In more complicated flow fields, the local strain direction may deviate significantly from the flow direction (e.g., Long, 2013). In contrast, under the high deviatoric stress, water-rich, and relatively low-temperature conditions of subduction-zone mantle wedges, B-type fabric may form, characterized by a slip system that produces fast polarization directions that are perpendicular to the flow (e.g., Kneller et al., 2005; Karato et al., 2008). With the exception of the mantle wedge corner, we do not expect B-type olivine fabric to play a substantial role in the interpretations of this study, and we generally assume that the fast polarization azimuth reflects the direction of present (or past) mantle deformation[e.g.,][]Song and Kawakatsu (2012); Faccenda (2014).

The alignment of fast splitting directions relative to the nearby subduction trench is commonly used to characterize subduction zone flow (e.g., Long and Silver, 2008; Song and Kawakatsu, 2012; Long, 2013). While trench-parallel fast directions are frequently observed (e.g., Long, 2013), they are often difficult to reproduce in geodynamic models away from horizontal or tangential, toroidal flow near slab edges, which can itself be oriented trench-parallel, (e.g., Alisic et al., 2012; Faccenda and Capitanio, 2013; Faccenda, 2014), or without assuming mechanical decoupling between the slab and the surrounding mantle (e.g., Paczkowski et al., 2014b). Models that include trench migration, with either trench rollback or advance, sometimes predict regions of trench-parallel extension beneath the subducting slab even when the dominant flow direction is trench-perpendicular (e.g., Faccenda and Capitanio, 2013). Various models have been proposed to explain trench-parallel fast splitting directions (e.g., Long and Silver, 2008; Song and Kawakatsu, 2012; Paczkowski et al., 2014a); however, they have yet to be fully understood and reconciled with geodynamic flow predictions.

In this study, we present shear-wave splitting measurements of PS and PPS seismic phases beneath the Philippine Sea Plate and within the surrounding subduction zones (Figure 1), a region characterized by sparse seismic station coverage. This approach enables us to investigate both the detailed anisotropy patterns associated with individual subduction systems and the

broader flow field within the upper mantle. Our results reveal that upper-mantle flow across much of the study region departs significantly from the direction of absolute plate motion (APM). Comparison with previous surface-wave studies further suggests that the observed splitting patterns primarily reflect seismic anisotropy originating from deep within the upper mantle. Our splitting results bear a striking resemblance to the geodynamic flow patterns predicted by global mantle circulation models (Alisic et al., 2012) that incorporate composite rheology and slab–mantle coupling.

2. Data

Our dataset includes all station-event combinations for earthquakes with magnitudes ≥ 5.9 from 2000 to October 2024, for which PS (at an epicentral distance from 90° to 115°) and PPS (115° to 135°) P-to-SV conversion points fall within our study region (Figure 1b), collected from 25 data centers worldwide (`http://adept.sese.asu.edu/`). Due to the unique configuration of earthquakes in our study region, PS and PPS sample the upper mantle in this region from multiple directions (Figure 1d), enabling a novel splitting intensity-based approach for estimating splitting parameters, described in Section 5. All data are corrected for instrument response, integrated to displacement, rotated to radial and transverse components, and downsampled to 20 samples per second.

3. Shear-wave splitting measurements

A shear wave that traverses an anisotropic medium splits into two components, one traveling relatively fast and the other slow (e.g., Vinnik et al., 1989; Silver and Chan, 1991). The time lag between these two components is referred to as δt and the polarization azimuth of the fast traveling wave (relative to north) is called ϕ.

A quantity that is often used to define the strength of splitting for a given phase on an individual seismogram is the splitting intensity (Chevrot, 2000), SI, defined as

$$SI = -2\frac{T(t)R'(t)}{|R'(t)|^2} \approx \delta t \sin[2(b-\phi)] \ , \tag{1}$$

where $R(t)$ is the radial component, $R'(t)$ is the time derivative of the radial component and $T(t)$ is the transverse component. The splitting intensity formula exploits the fact that, in the case of shear-wave splitting of radially polarized waves (such as PS, PPS, SKS, PKS and SKKS), for periods that are large relative to the splitting delay time, the transverse component

waveform is directly proportional to the time derivative of the radial component waveform (e.g., Silver and Chan, 1991; Chevrot, 2000).

We determine splitting parameters for PS, PPS and core-refracted phases using a version of SplitRacerAUTO (Reiss and Rümpker, 2017; Link et al., 2022), which implements the transverse energy minimization technique (Silver and Chan, 1991) including the corrected uncertainty calculation from Walsh et al. (2013). All data are bandpass-filtered to retain periods between 6 and 25 s. For detailed benchmarks for our automated splitting approach, we refer to Link et al. (2022) and Wolf et al. (2025).

4. Complementary measurements from core-refracted waves

As complementary information for our PS and PPS measurements, we use SKS splitting results from the compilation of Becker et al. (2012) (Figure 2c). Although some influence from the lowermost mantle may exist (e.g., Wolf et al., 2024b,c), such SKS phases are mostly sensitive to seismic anisotropy in the upper mantle (e.g., Sieminski et al., 2008; Wolf et al., 2024a). Additionally, for some ocean island stations that are not included in the compilation of Becker et al. (2012), we determine station-averaged PKS, SKS and SKKS (*KS, i.e., phases ending in "KS", Figure 1a) splitting to complement our PS and PPS splitting measurements (Section 5). These station-averaged measurements are shown in Table 1.

Table 1: Station-averaged splitting measurements conducted using core-refracted waves.

Station	Network	Lat (°)	Lon (°)	ϕ (°)	95% range (°)	δt (s)	95% range (s)	Number
JMZ	JP	25.82	131.22	48	9/72	1.5	0.34/2.87	3
SAP4	XO	15.17	145.77	32	12/76	1.2	0.55/2.5	1
SAP3	XO	15.18	145.75	32	14/60	1.8	0.79/2.90	3
SAIP	SS	15.21	145.75	33	12/55	0.8	0.33/1.70	2
DAV	IU	7.07	125.58	-27	-56/-12	1.3	0.52/2.15	4
SZP	RM	17.55	120.46	-44	-83/-14	1.4	0.42/3.70	2
BAG	PS	16.41	120.58	-37	-74/-12	1.1	0.41/2.2	1

5. Constraining seismic anisotropy using PS and PPS data

Core waves with P-to-SV conversions at the core exit location, such as SKS, PKS or SKKS (Figure 1a), are commonly used to infer seismic anisotropy (primarily) in the upper mantle

beneath the station (e.g., Savage, 1999; Long and Silver, 2009). PS and PPS phases sample similar upper mantle anisotropy as SKS and SKKS beneath the station; however, they have an additional shear-wave leg through the upper mantle after converting from P-to-SV upon reflection at the surface (Figure 1a). Therefore, the measured anisotropy from PS-SKS and PPS-SKKS phase pairs can be used to infer seismic anisotropy at the PS and PPS P-to-SV conversion point (Su and Park, 1994; Wolf and Long, 2023; Wolf et al., 2024d).

Importantly, PS and PPS splitting near their P-to-SV conversion point is accumulated on the downgoing leg of the raypath, implying that the residual PS and PPS splitting measurement (after accounting for receiver-side anisotropy) needs to first be translated into the P-to-SV conversion point reference frame (Wolf and Long, 2023). Therefore, for PS, ϕ_R, which is the fast azimuth measured at the station, is converted into the geographic reference frame of the conversion point (Wolf and Long, 2023).

We measure ϕ_R, δt, and SI values for PS and PPS phases using SplitRacerAuto (Section 3). For PS, we use epicentral distances between 90° and 115°, and for PPS between 115° and 135°. At these distances, the S leg turning location of PS and PPS is more than 250 km above the core–mantle boundary (Figure 1a), minimizing any potential contribution from lowermost mantle anisotropy. As different PS and PPS phases sample the lowermost mantle at distinct geographic locations, any residual full-wave sensitivity to anisotropy is unlikely to create a systematic, backazimuth-dependent signal, and we rely on backazimuthal variations to derive the splitting parameters for most of our measurements (see below).

We infer shear-wave splitting parameters using two different approaches. First, in cases in which *KS splitting is null for the same source-receiver pair or if PS splitting is measured at previously classified null stations (Wolf et al., 2025), PS splitting can directly be attributed to the PS bounce point. These are retained if classified as 'good' or 'average', with classification criteria including error thresholds for δt, minimum energy reductions for corrected traces, and eigenvalue ratio requirements for the covariance matrix being the same as those tested in detail in Wolf et al. (2025). This procedure has been shown to be effective, as incidence angles of surface-reflected and *KS waves are sufficiently similar near the receiver so that similar anisotropy is sampled (Wolf and Long, 2023). Specifically, for a source depth of 500 km, *KS incidence angles at the receiver would be between 4° and 12° for the distance range used, whereas PS and PPS waves have angles of incidence between 15° and 18°. An example measurement for which PS is strongly split (and SKS splitting is null) is shown in Figure 2b. We apply the same procedure to PPS for this first approach, but obtain no measurements.

Second, we bin PS and PPS P-to-SV conversion points and determine differential PS-SKS or PPS-SKKS splitting intensities for every bin, thereby explicitly correcting for receiver-side anisotropy. Overall, 93% of our measurements rely on PS and 7% on PPS waves. To assure the high quality of the measurements, we only use PS-SKS and PPS-SKKS splitting intensity residuals for events (a) with a signal to noise ratio of 3.5 for both phases; (b) if the correction of the splitting during the individual analysis of the PS phases leads to a reduction of transverse energy of at least 30% for phases with considerable splitting (if the corresponding absolute splitting intensity larger than 0.3), and (c) for which the absolute splitting intensity is smaller than the inferred splitting time for the individual phase. The binning is performed on a equidistant spatial grid of 0.25°. At each bin centered at the grid point, we consider differential splitting intensity values with P-to-SV conversion points at a maximum distance of d_b, described below. We allow this distance to vary depending on the azimuthal coverage of the PS and PPS phases within the volume around each grid point. We seek an azimuthal coverage of at least 40% in a modulo 180° backazimuthal range. This is achieved by first, projecting all measurements arriving from a backazimuth larger than 180° to the first 180° interval ($baz_{proj} = baz - 180°$). This is valid in case of a single homogeneous anisotropic layer underneath the point of interest. Subsequently, we inspect histograms of the azimuthal distribution in 10° bins. The azimuthal coverage is determined by the number of bins occupied by one or more measurements relative to the total number of intervals. We seek a coverage of at least 7 bins of a total of 18 for azimuthal increments of 10°. The distance limit d_b is varied, starting at 1.5° with 0.5° increases until this criterion is fulfilled or a maximum distance limit of 4 degrees is exceeded. In the latter case, the grid point is considered insufficiently sampled and is not used in the analysis. The assembled splitting intensity residuals at each grid point are averaged in 10° azimuthal bins. We discard outliers (measurements that exceed one standard deviation around the group's mean) and estimate the average and error for each azimuthal group as basis for the subsequent analysis step (Figure 2b).

All shear-wave splitting measurements used in this study, including PS and PPS phases and complementary measurements from core-refracted phases, are presented in Figure 2c. This panel also provides the geographic context for the example measurements shown in Figure 2a and Figure 2b.

6. Fast directions relative to the nearest trench

Our PS and PPS shear-wave splitting results are shown in Figure 3. We find widespread fast splitting directions that are parallel to the nearest subduction trench for most fore- and backarcs in our study region, although there are exceptions in parts of the Mariana and Izu-Bonin subduction zones (Figure 3). Fast direction azimuths just outboard of the trenches, which likely reflect deformation beneath the subducting slab, tend to be trench-perpendicular beneath the Pacific Plate, but consistently trench-parallel beneath the Philippine Sea Plate (Figure 3). Fast splitting directions in the southwest of our study region are primarily oriented in northwest-southeast direction, but are hard to interpret in terms of trench-parallel/perpendicular splitting due to complicated subduction zone arrangement (Figure 3).

7. Depth and geometry of seismic anisotropy

The simplest possible geodynamic model for our study region would predict convergence-parallel (generally trench-perpendicular) fast directions near subducting slabs, with APM-parallel fast directions beneath the Philippine Sea Plate interior. Notably, however, our measurements generally do not align with the direction of APM (Figure 4c) or with convergence directions (Figures 3 and 6). This implies that either flow in the asthenosphere is unlike what would be predicted based on simple assumptions above, or that the dominant seismic anisotropy contribution is not located at asthenospheric depths.

Our measurements could potentially be influenced by frozen-in seismic anisotropy in the oceanic lithosphere (Figure 4a). As new lithosphere forms at mid-ocean ridges, it initially records the spreading direction at the time of formation. Such a correlation between shallow anisotropy fast directions and ancient spreading directions, approximated here as the gradient in seafloor age (Figure 4b), has been documented for seafloor up to an age of ∼100 Myr (e.g., Becker et al., 2014). We therefore test for such a correlation, but no such general correlation is observed (Figure 4d), indicating that lithospheric anisotropy does not exert a dominant influence on our measurements. This is also supported by our comparison of our fast polarization directions from shear-wave splitting to those obtained from surface waves that are primarily sensitive to lithospheric depths (e.g., Figure 5a).

While surface waves have coarser lateral resolution compared to body wave shear-wave splitting, they offer superior depth resolution of seismic anisotropy. We therefore compare our measured fast polarization directions to those from two azimuthal anisotropy models inferred

from surface waves (Debayle et al., 2016; Schaeffer et al., 2016) to constrain the depths of anisotropy that the measured body wave splitting most likely reflects. Strikingly, our measurements agree best with fast polarization directions from surface wave models over a depth range between 250 and 400 km (Figure 5), especially for the northeastern part of our study region. These results suggest that the measured shear-wave splitting across our study region dominantly reflects seismic anisotropy deep in the upper mantle, while some local contributions of shallower anisotropy cannot be excluded in the west of our study region.

Importantly, PS and PPS phases have near-vertical incidence angles and therefore primarily resolve azimuthal anisotropy (that is, wavespeed variations in the horizontal plane). Consequently, tilted anisotropy associated with shallowly subducting slabs, such as those beneath Japan or the Izu–Bonin region, or with non-horizontal mantle flow near slabs would manifest as a projection onto the horizontal plane (e.g., Song and Kawakatsu, 2012). While direct measurements backazimuth-dependent (ϕ, δt) from core-refracted phases or direct PS can, in principle, resolve tilted anisotropy, our approach, mainly based on differential splitting intensities as a function of backazimuth, is not sensitive to such effects. This is particularly true given that the backazimuthal coverage, though as complete as possible for this region, remains limited (Figure 1d). Similarly, because our method primarily relies on the backazimuthal variation of splitting intensity differences, sorting measurements by whether a raypath samples a potential slab would not enable the inference of splitting parameters, as this would not give the directional coverage required to infer splitting parameters. It is thus important to keep in mind that our analysis is not capable of directly resolving tilted anisotropy or the effects of anisotropy within subducting slabs themselves.

8. Comparison with previous shear-wave splitting constraints

8.1. SKS splitting

Due to the lack of seismic stations in our study regions, typical *KS splitting constraints are sparse; however, wherever *KS splitting measurements have been acquired, we expect a general agreement between PS and PPS (ϕ, δt)-values inferred from SI with those that have been measured directly, and with *KS measurements. In case of small-scale heterogeneity in anisotropy, perfect agreement is not expected, as SI-inferred (ϕ, δt)-values are laterally averaged. Overall, surface-reflected and *KS splitting measurements are in good agreement with one another (Figure 3a). Additionally, our PS and PPS splitting measurements agree

with previously measured SKS splitting (Long and van der Hilst, 2005, 2006) near the Nankai and Ryuku subduction zones.

8.2. Local S splitting in subduction systems

Splitting measurements of local S phases originating from earthquakes within subducting slabs mainly sample anisotropy within the mantle wedge. They are not, therefore, directly comparable to our PS and PPS measurements, which sample the entire upper mantle. However, comparison of splitting from different types of seismic phases can shed light on the depth distribution of anisotropy in subduction zones (Long and Silver, 2008; Long and Silver, 2009).

Wirth and Long (2010) observed trench-oblique splitting near Izu-Bonin, in agreement with our results. Additionally, the shear-wave splitting measurements conducted by Wang and He (2020) for the southwest of our study region are consistent with our measurements, despite the different sensitivity of the seismic phase (sS) that they used. Previously detected trench-parallel fast directions detected in the mantle wedge near the Marianas (Pozgay et al., 2007) are partially confirmed, although we show some trench-perpendicular measurements in the forearc. This apparent disagreement is likely explained by the fact that Pozgay et al. (2007) applied local splitting measurements and are therefore only sensitive to seismic anisotropy in the wedge, whereas our PS and PPS waves traverse the whole upper mantle underneath. Furthermore, the PS-based fast directions are obtained using a binning approach (Section 5), making them less sensitive to small-scale lateral variations than the measurements by Pozgay et al. (2007).

8.3. Source-side splitting measurements of sub-slab anisotropy

Teleseismic S waves can be used to infer sub-slab anisotropy in the upper mantle beneath the earthquake source (e.g., Russo et al., 2010). Due to their different upper mantle raypaths compared to core-refracted and surface-reflected seismic phases, perfect agreement is not necessarily expected. Source-side S measurements near Izu-Bonin generally show trench-oblique fast directions (Lynner and Long, 2014, 2015), in agreement with our PS and PPS measurements. In the northernmost part of the Izu-Bonin subduction zone, a rotation of fast splitting directions is indicated by Lynner and Long (2015), which is also seen using PS and PPS. Near Ryuku, we find generally trench-parallel fast directions, in agreement with Long and van der Hilst (2006), but contrary to Lynner and Long (2014), although some smaller-scale complexity exists. For the Japan subduction zone, measurements from teleseismic S waves generally suggest trench-parallel fast directions (Lynner and Long, 2014), but for this region no splitting parameters are obtained in this study.

9. Geodynamic implications

Our shear-wave splitting measurements provide constraints on both local subduction-induced deformation and, collectively, on the broader flow patterns within our study region. The fast polarization direction observed in the upper mantle beneath and surrounding the Philippine Plate align most closely with previous surface-wave results for depths between 250 and 400 km, suggesting that our splitting measurements primarily reflect flow at these depths. As mentioned above, the simplest possible geodynamic model for our study region would predict convergence-parallel fast directions near subducting slabs, and APM-parallel fast directions beneath the Philippine Sea Plate interior. Notably, our measurements generally do not align with the direction of APM or with convergence directions (Figures 3 and 6). Our measurements represent azimuthal anisotropy projected onto the horizontal plane (Section 7). Because our method is less sensitive to anisotropy caused by non-horizontal flow, our interpretations primarily focus on horizontal flow patterns. Nevertheless, a substantial vertical component of mantle flow may be present in the vicinity of subducting slabs. Furthermore, trench rollback or advance may induce local extension directions that are not parallel to the flow direction (e.g., Faccenda and Capitanio, 2013), potentially complicating interpretations directly adjacent to subducting slabs.

9.1. Implications for subduction zone anisotropy and flow

Our measurements reveal clear patterns of trench-parallel and trench-perpendicular fast directions in several subduction systems within our study area. In the Ryukyu subduction zone, we observe trench-parallel fast directions on the arc side of the trench, similar to previous studies (Long and van der Hilst, 2005, 2006). Possible explanations for this include B-type olivine fabric in the shallow mantle wedge corner (Kneller et al., 2005), seismic anisotropy within the slab or associated with non-horizontal mantle flow, as well as a component of trench-parallel mantle flow either above or beneath the subducting slab. Such three-dimensional flow can be induced by trench rollback, or may reflect background mantle flow directions (e.g., Paczkowski et al., 2014b). Ryukyu also displays trench-parallel fast directions on the outboard side of the trench; these measurements are not sensitive to anisotropy in the mantle wedge above the slab, and therefore likely reflect flow beneath the slab itself, although more complicated effects of non-horizontal flow are a possibility. Alternatively, slab rollback can induce trench-parallel extension, causing trench-parallel anisotropy, even when the flow itself is dominantly trench-perpendicular (e.g., Druken et al., 2011; Alisic et al., 2012; Faccenda and Capitanio, 2013; Crameri and Tackley, 2014; Paczkowski et al., 2014b).

Trench-parallel fast directions also dominate on both sides of the Philippine trench; given the highly oblique convergence directions here (Figure 1), these may indicate convergence-parallel shear, trench-parallel flow, a combination, with a possible role for B-type fabric in the shallow mantle wedge, or internal slab anisotropy. The southern Izu-Bonin and Mariana arcs show coherent trench-parallel fast directions on the arc side of the trench, consistent with previous work (Pozgay et al., 2007; Wirth and Long, 2010). The fact that these extend well into the backarc suggest a role for trench-parallel flow; they cannot be solely due to B-type fabric in the forearc wedge, although a non-horizontal flow component near the slab may play a role. Such trench-parallel flow may be driven by toroidal flow around the slab edge in the Southern Marianas, which may have been responsible for causing the slab to migrate, causing the arcuate geometry of the Marianas trench (e.g., Crameri and Tackley, 2014). The northern part of Izu-Bonin and the Japan subduction zone exhibit convergence-parallel fast directions, consistent with the simplest model for subduction zone flow (e.g., Long, 2013). Strikingly, fast directions on the outboard side of the Mariana subduction zone trend consistently northeast-southwest, a direction that is oblique to both the absolute plate motion direction of the Pacific Plate and the convergence direction. This direction is nearly trench-perpendicular in the northern portion of the arc, but oblique to the trench strike in its southern portion. These directions are not easily explained by either slab-driven entrained flow, by a toroidal flow model, or by seismic anisotropy within the slab, due to the steep subduction angle in this region; instead, they may reflect the ambient, large-scale mantle flow field, likely in the absence of viscous coupling between the slab and the mantle beneath, and without significant deflection of the flow by the slab itself (e.g., Paczkowski et al., 2014b).

9.2. Regional-scale flow patterns

Splitting measurements that sample the mantle directly adjacent to subducting slabs reflect the local subduction-induced flow field. With our dataset, we are also able to interrogate the drivers of mantle flow beneath the Philippine Sea Plate itself, which is bounded on all sides by subduction zones. While the simplest possible model for this flow invokes plate motion parallel shearing in the asthenospheric upper mantle, driven by plate motion, an alternative hypothesis is that mantle flow is instead controlled by regional-scale subduction dynamics, with the surrounding slabs driving flow on both a local scale (adjacent to the slabs) and on a regional scale (e.g., Link and Rümpker, 2023). To test this hypothesis, we investigate the global mantle flow models of Alisic et al. (2012), who computed flow models with realistic plates using an adaptive

finite element approach, specifically focusing on the influence of subduction on flow dynamics. They conducted a detailed analysis of predicted mantle flow patterns within our study region, also for depth deep in the upper mantle, for which our inferred fast polarization directions agree best with those inferred from surface waves (Figure 5). Their predicted horizontal flow velocities at 400 km depth show remarkable agreement with the fast axis orientations inferred from our splitting measurements (Figure 6), particularly in the areas that are not directly adjacent to downgoing slabs, in which a vertical flow component may play a larger role in causing seismic anisotropy, and fabrics may therefore be tilted. Consistent with the predictions of Alisic et al. (2012), we find evidence for toroidal flow around the southern edge of the Mariana slab (Figure 6, slice C), which drives flow to the north beneath the Philippine Sea Plate. Their model also predicts toroidal flow around the northern edge of the Philippine subduction zone, consistent with our observations (which are relatively sparse in this area). The global flow model also predicts flow beneath the Pacific Plate, just outbound of the Mariana trench, in a direction that is nearly parallel to our fast splitting directions. Finally, just west of the Ryukyu slab, the model of Alisic et al. (2012) predicts flow that is directed to the east and appears to be deflected to the northeast by the slab itself, providing one potential explanation for the nearly trench-parallel fast directions in the Ryukyu backarc (Figure 6, slice A). We additionally see evidence for an (almost) circular splitting pattern, apparently induced by the arc of the Mariana Slab (Figure 6, red arrows in main panel), which is not indicated by the Alisic et al. (2012) model. The flow could be clockwise if viscous coupling of flow from the southern edge of trench is driving it, or counterclockwise if flow to the north on the west side of the trench is pulling the material. It may alternatively be related to extension, linked to the arcuate shape of the Marianas subduction zone Kneller and van Keken (2008); Crameri and Tackley (2014)

In general, our splitting observations, and the favorable comparison between the mantle flow model of Alisic et al. (2012), highlights the clear importance of subducting slabs in controlling regional-scale mantle flow. This is true even in the central portion of the Philippine Sea plate, which is not directly adjacent to a subduction trench but which does exhibit a flow field that is driven by regional-scale toroidal flow around a slab edge. This observation demonstrates that the simplest model of plate motion driven flow in the asthenosphere beneath the interiors of tectonic plates likely only holds in regions far away from plate boundaries. Slabs, known to influence nearby flow, also play key roles in controlling flow patterns on the order of 1000 km away from subduction zone trenches, as proposed by Alisic et al. (2012) based on numerical modeling.

10. Conclusions

We have developed a novel strategy that relies on splitting intensity measurements of PS and PPS phases to infer shear-wave splitting parameters in regions lacking station coverage and applied this technique to investigate seismic anisotropy within and surrounding the Philippine Sea Plate. The observed seismic anisotropy primarily reflects mantle flow at upper mantle depths, between 100 and 400 km, and is strongly influenced by the surrounding subduction zones. We find widespread trench-parallel flow in the mantle wedge of the Ryukyu, Nankai, and parts of the Izu-Bonin subduction zones, as well as evidence for toroidal flow around the edges of the Ryukyu and Mariana slabs. Beneath the Pacific Plate, in the Mariana subduction zone, flow is predominantly trench-perpendicular. Beneath the interior of the Philippine Sea Plate itself, fast directions are not parallel to APM, as predicted by the simplest models, but are instead controlled by regional-scale subduction driven flow. This study demonstrates the power of PS and PPS splitting for studying poorly instrumented oceanic subduction zones, allowing us to augment existing global databases of subduction zone anisotropy measurements (e.g., Long and Silver, 2009; Long and Wirth, 2013) and shedding new light on subduction zone geodynamics.

Data availability

All data used in this study are publicly available and were collected and pre-processed as part of ASU's global data collection system for their global data products project (`http://www.adept.science`). More details are specified in the Supplementary Information.

Data were collected from the following on-line data centers: BGR (`https://eida.bgr.de/`), CNDC (`https://www.earthquakescanada.nrcan.gc.ca/stndon/CNDC/index-en.php`), Earthscope (`http://service.iris.edu/`), ETH (`https://eida.ethz.ch/`), GEOFON (`https://geofon.gfz-potsdam.de/`) GFZ Data Services (1993), ICGC (`https://www.icgc.cat/en/Ciutada/Explora-Catalunya/Terratremols`), INGV (`http://cnt.rm.ingv.it/en/webservices_and_software`), IPGP (`http://ws.ipgp.fr/`) Institut de physique du globe de Paris (IPGP) and École et Observatoire des Sciences de la Terre de Strasbourg (EOST) (1982), KNMI (`http://rdsa.knmi.nl/`), KOERI (`http://www.koeri.boun.edu.tr/new/en`), LMU (`http://erde.geophysik.uni-muenchen.de/`), NCEDC (`https://ncedc.org/`) UC Berkeley Seismological Laboratory (2014), NIEP (`https://www.infp.ro/`), NOA (`http://bbnet.gein.noa.gr/HL/`), OHPDMC (`http://ohpdmc.eri.u-tokyo.ac.jp/`), ORFEUS (`http://www.orfeus-`

eu.org/), RESIF (https://seismology.resif.fr/) RESIF (1995), SCEDC (https://scedc.caltech.edu/)Caltech (2014), SSN (http://www.ssn.unam.mx/) Instituto de Geofísica, Universidad Nacional Autónoma de México, México (2024), and TEXNET (http://rtserve.beg.utexas.edu/). All networks and network citations are included as Supplementary Information, and were derived from the FDSN network code list (https://fdsn.org/networks/).

Code availability

The Generic Mapping Tools (Wessel and Smith, 1998), ObsPy (Beyreuther et al., 2010), and SplitRacerAuto (Link et al., 2022) were utilized in this study.

Acknowledgements

JW was funded by the Miller Institute for Basic Research in Science at UC Berkeley. MDL, EG and JDW received funding from the US National Science Foundation (NSF) via grants EAR-2153688, EAR-2348594 and EAR-1853911. JW thanks Weiqiang Zhu for providing the computational resources necessary for this study, and the Berkeley seismology group for helpful discussions. We thank Manuele Faccenda, Zhouchuan Huang, and an anonymous reviewer for insightful comments that helped us to improve the paper.

Competing Interests

The authors are not aware of any competing financial or personal interests that could have influenced the work reported in this paper.

Figures

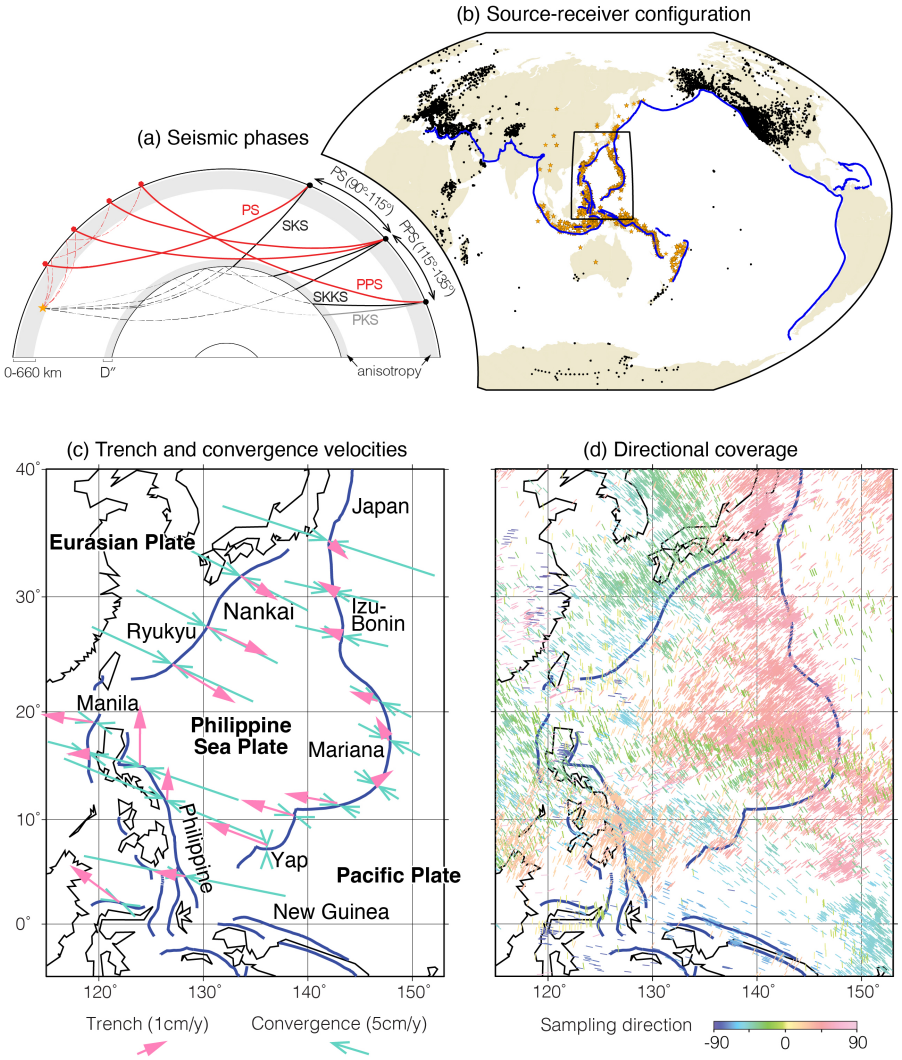

Figure 1: Seismic phases used in this study and source-receiver configuration. (a) Cross-section of Earth's interior illustrating raypaths from event (yellow star) to receiver (black circle) for SKS, SKKS (black lines), PKS (gray line), PS and PPS (red lines). The part of the raypath for which seismic anisotropy is characterized via shear-wave splitting is shown as a solid line. Distance ranges used for PS and PPS are indicated. PS and PPS surface P-to-SV conversion points are shown as red hexagons. Mantle regions characterized by substantial anisotropy are indicated by gray shading. (b) Earthquakes (yellow stars) and seismic stations (black circles) used in this study. The study region is shown as a black rectangle. (c) Zoom-in to our study region with naming conventions and trench (in NNR frame, Heuret and Lallemand, 2005) and convergence (inferred from GSRM v2.1 in NNR frame, Kreemer et al., 2014) velocities shown as arrows (legend, NNR=No-Net-Rotation). (d) Coverage of our study region shown by sticks, oriented in sampling direction, centered at the PS and PPS P-to-SV conversion points. Colors also indicate sampling direction (legend).

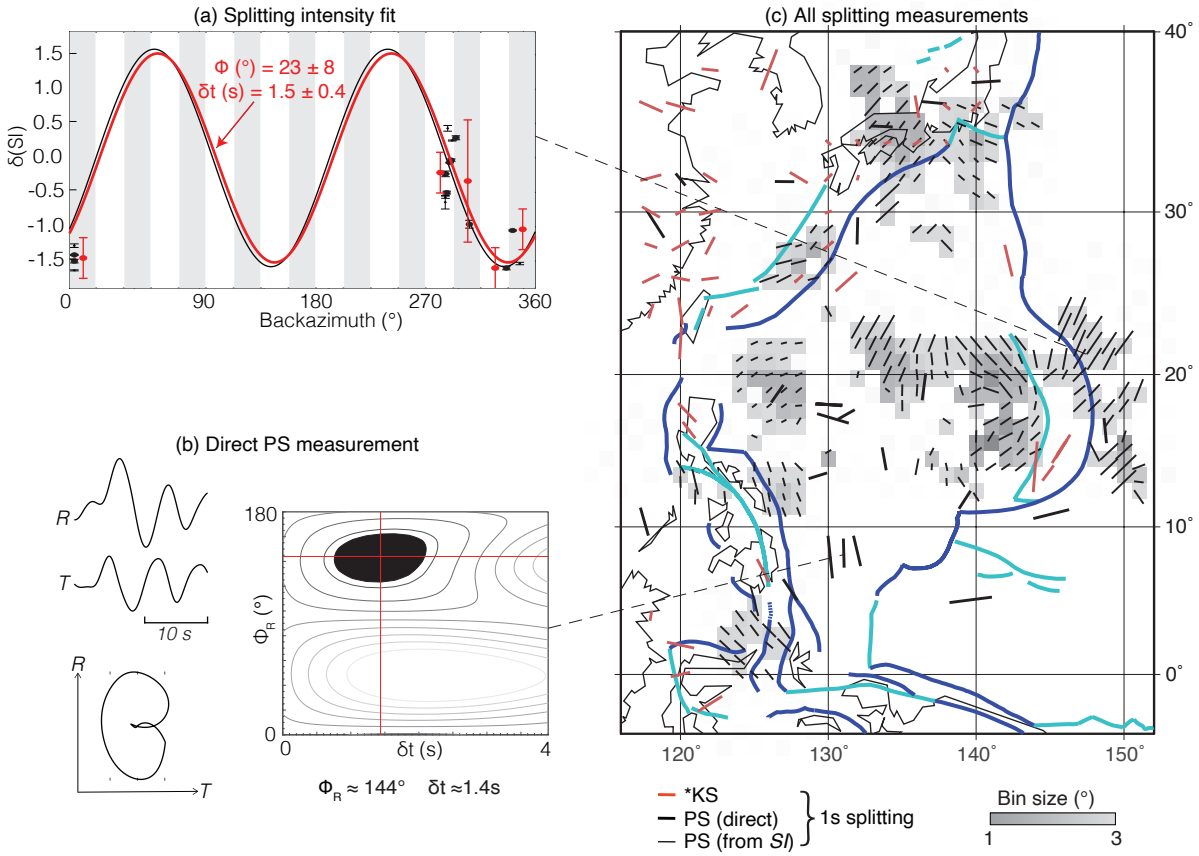

Figure 2: Real-data splitting examples and results. (a) Example $\sin(2\theta)$-fits (Equation (1)) for a single bin (see panel header) used to determine (ϕ, δt) from differential PS-SKS and PPS-SKKS splitting intensity measurements. Fits are shown for single measurements (black) and 18° backazimuthal bins (red). (b) PS Splitting example for an event that occurred on December 5, 2016, recorded at seismic station N30M. Radial (R) and transverse (T) waveforms (top left), particle motion (bottom left) and $\phi - \delta t$-grid right, where the black region denotes the 95% confidence interval and the red cross marks the best-fitting splitting parameters. (c) Splitting measurements (ϕ, δt) are represented by lines (legend), with PS-derived measurements shown in black (thick lines: direct measurements; thin lines: inferred from SI) and *KS measurements in red. 2° SKS splitting averages from Becker et al. (2012) (last accessed 03/2025) are shown, supplemented with *KS measurements from ocean island stations (Supplementary Table S1). Gray background shading indicates the bin size for (ϕ, δt) inferred using SI (legend). Dark blue lines mark subduction zone trenches and light blue lines denote spreading and transform boundaries (Bird, 2003).

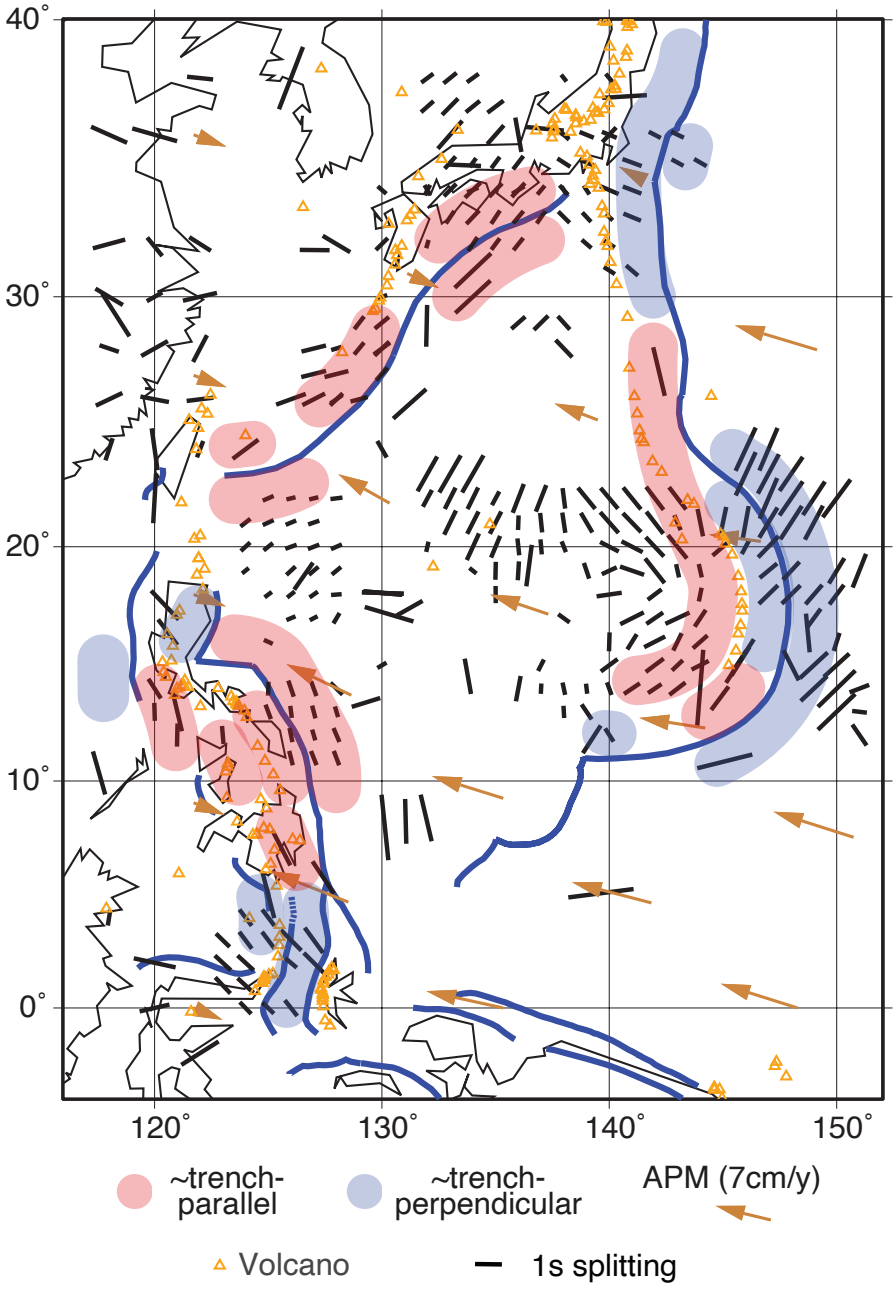

Figure 3: Predominantly trench-parallel (red shading) and -perpendicular (blue shading) shear-wave splitting fast directions. Dark blue lines mark subduction zone trenches (Bird, 2003), and volcano locations (`ngdc.noaa.gov/hazard/`) are indicated by yellow triangles. APM are shown (legend, Kreemer et al., 2014).

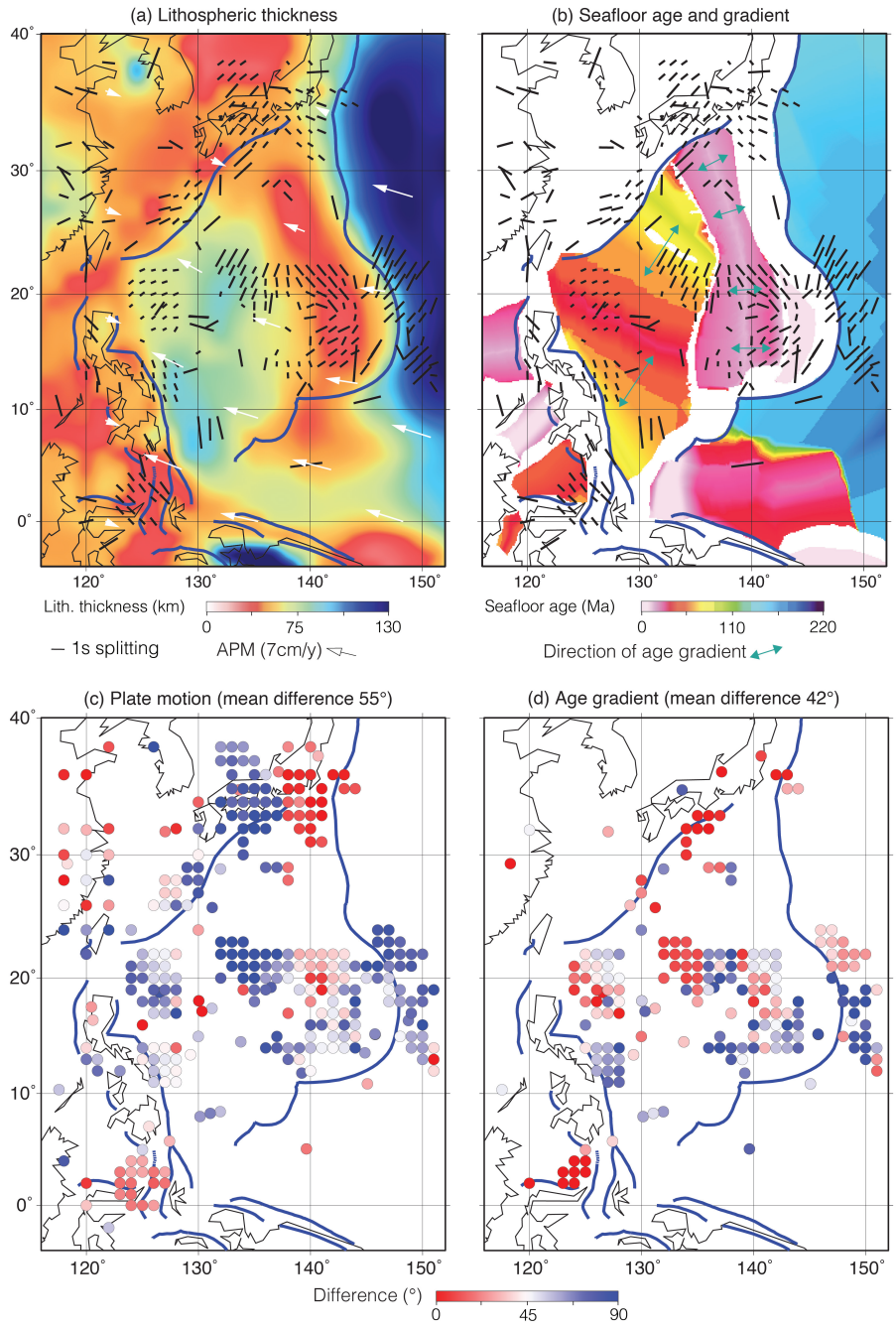

Figure 4: Test of the hypothesis that observed shear-wave splitting is either due to primarily asthenospheric flow in APM direction, or due to frozen-in anisotropy in the lithosphere. (a) Splitting measurements (legend), APM directions (legend, Kreemer et al., 2014), and on top of the mean lithospheric thickness model of Steinberger and Becker (2018). (b) Similar to panel (a) showing seafloor age (legend, Müller et al., 2019) and age gradient (turquoise arrows). (c) Difference of fast splitting directions (legend) to APM. The mean difference is 55°. (d) Same as panel (c) for the gradient of seafloor age, with a mean difference of 42°.

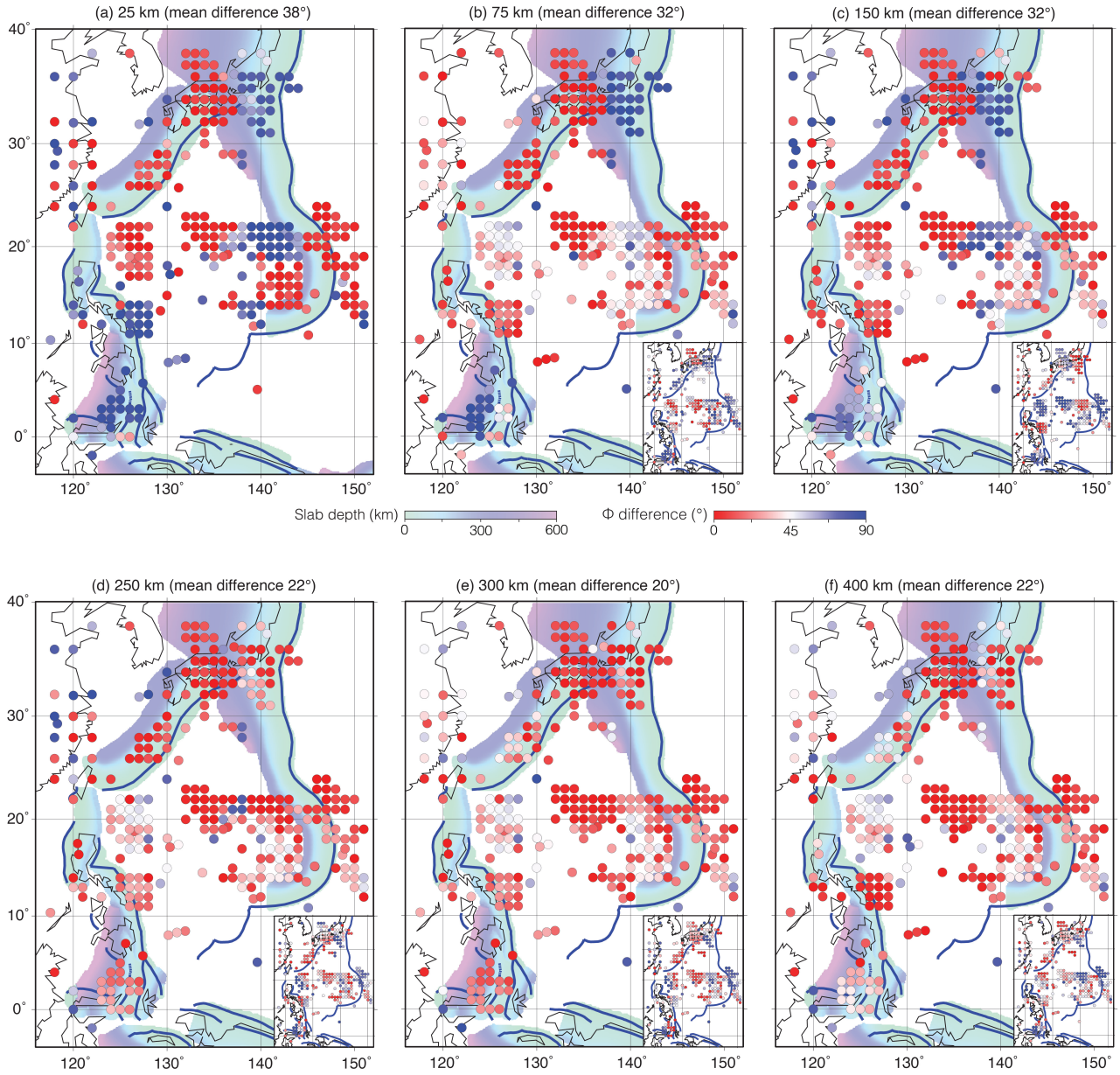

Figure 5: Comparison of fast polarization directions from our shear-wave splitting measurements (legend) with the surface wave-based models by Schaeffer et al. (2016) (main panels) and Debayle et al. (2016) (insets) for depth slices at (a) 25 km, (b) 75 km, (c) 150 km, (d) 250 km, 300 km, and 400 km. Debayle et al. (2016) does not report results for 25 km depth. Trench locations (Bird, 2003) are indicated by blue lines. The background colors represent slab depth (legend) based on Slab2 (Hayes et al., 2018).

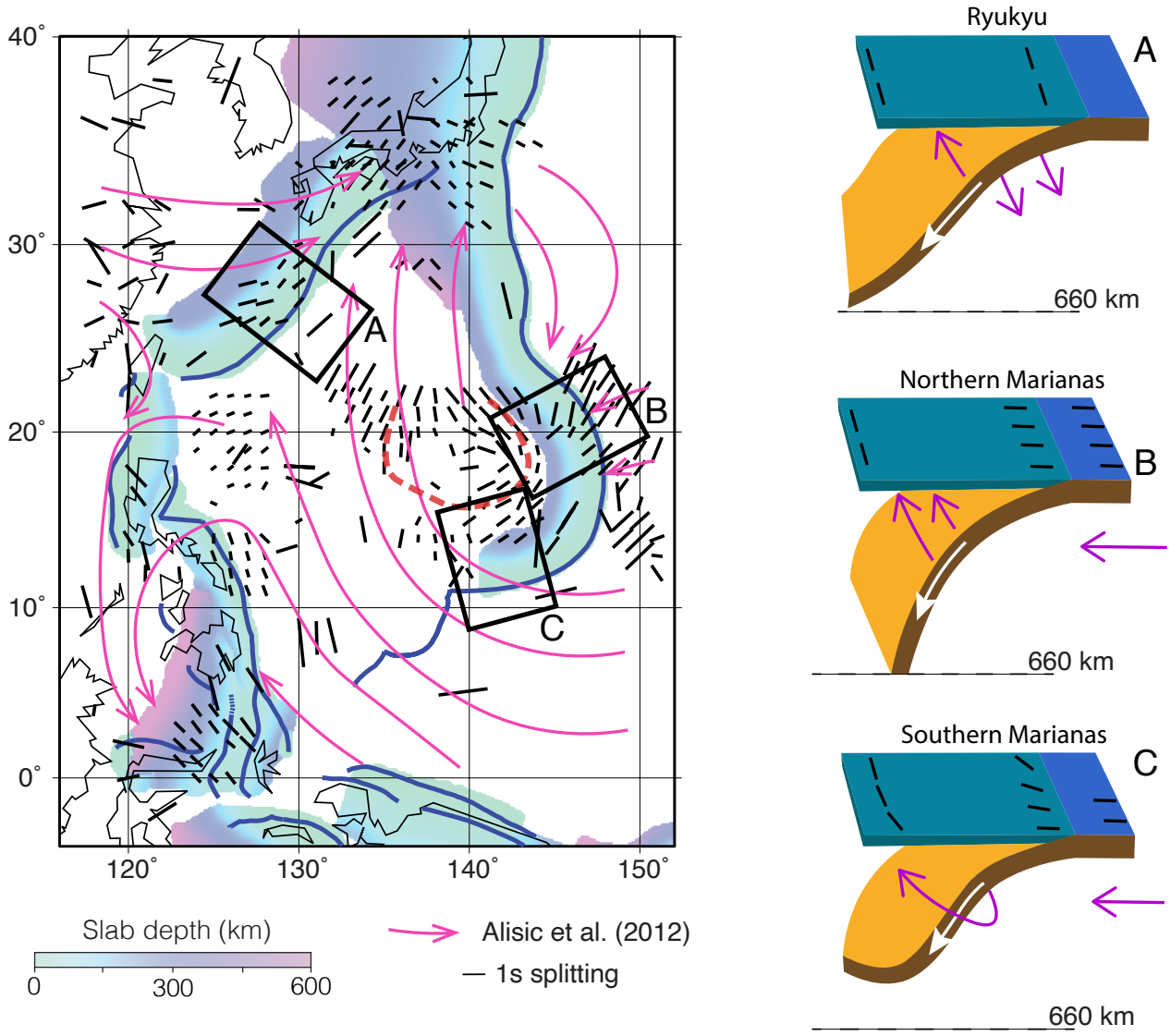

Figure 6: Geodynamic interpretation of our measurements. Main panel: PS and SKS shear-wave splitting measurements, APM from Kreemer et al. (2014), and geodynamically derived flow patterns at 400 km depth from Alisic et al. (2012) (legend). Toroidal flow due to the arc of the Mariana slab is shown by the dashed red dashed line. The background colors represent slab depth (legend) based on Slab2 (Hayes et al., 2018). Surface locations of cross-sections (A–C) are indicated, with schematic representations of likely flow patterns surrounding the main panel. Schematic flow diagrams: The subducting plate is depicted in dark blue, the overriding plate in light blue, and slabs in yellow. Flow directions are indicated by magenta arrows, while shear-wave splitting directions measured at the surface are shown as black sticks. Slab geometries are inspired by Fukao and Obayashi (2013).

References

Alisic, L., Gurnis, M., Stadler, G., Burstedde, C., Ghattas, O., 2012. Multi-scale dynamics and rheology of mantle flow with plates. Journal of Geophysical Research: Solid Earth 117. doi:10.1029/2012JB009234.

Becker, T.W., Conrad, C.P., Schaeffer, A.J., Lebedev, S., 2014. Origin of azimuthal seismic anisotropy in oceanic plates and mantle. Earth and Planetary Science Letters 401, 236–250. doi:https://doi.org/10.1016/j.epsl.2014.06.014.

Becker, T.W., Lebedev, S., Long, M.D., 2012. On the relationship between azimuthal anisotropy from shear wave splitting and surface wave tomography. Journal of Geophysical Research: Solid Earth 117, B01306. doi:10.1029/2011JB008705.

Beyreuther, M., Barsch, R., Krischer, L., Megies, T., Behr, Y., Wassermann, J., 2010. Obspy: A python toolbox for seismology. Seismological Research Letters 81, 530–533. doi:10.1111/10.1785/gssrl.81.3.530.

Bird, P., 2003. An updated digital model of plate boundaries. Geochemistry, Geophysics, Geosystems 4. doi:10.1029/2001GC000252.

Caltech, 2014. Southern California Earthquake Center. doi:10.7909/C3WD3xH1.

Chevrot, S., 2000. Multichannel analysis of shear wave splitting. Journal of Geophysical Research: Solid Earth 105, 21579–21590. doi:10.1029/2000JB900199.

Crameri, F., Tackley, P.J., 2014. Spontaneous development of arcuate single-sided subduction in global 3-d mantle convection models with a free surface. Journal of Geophysical Research: Solid Earth 119, 5921–5942. doi:https://doi.org/10.1002/2014JB010939.

Debayle, E., Dubuffet, F., Durand, S., 2016. An automatically updated S-wave model of the upper mantle and the depth extent of azimuthal anisotropy. Geophysical Research Letters 43, 674–682. URL: https://doi.org/10.1002/2015GL067329.

Druken, K.A., Long, M.D., Kincaid, C., 2011. Patterns in seismic anisotropy driven by rollback subduction beneath the High Lava Plains. Geophysical Research Letters 38, L13310. doi:10.1029/2011GL047541.

Faccenda, M., 2014. Mid mantle seismic anisotropy around subduction zones. Physics of the Earth and Planetary Interiors 227, 1–19. doi:10.1016/j.pepi.2013.11.015.

Faccenda, M., Capitanio, F.A., 2013. Seismic anisotropy around subduction zones: Insights from three-dimensional modeling of upper mantle deformation and SKS splitting calculations. Geochemistry, Geophysics, Geosystems 14, 243–262. doi:10.1002/ggge.20055.

Fan, J., Zhao, D., 2019. P-wave anisotropic tomography of the central and southern philippines. Physics of the Earth and Planetary Interiors 286, 154–164. doi:10.1016/j.pepi.2018.12.001.

Fan, J., Zhao, D., Li, C., Liu, L., Dong, D., 2024. Remnants of shifting early cenozoic pacific lower mantle flow imaged beneath the philippine sea plate. Nature Geoscience 17, 347–352. doi:10.1038/s41561-024-01404-6.

Fukao, Y., Obayashi, M., 2013. Subducted slabs stagnant above, penetrating through, and trapped below the 660 km discontinuity. Journal of Geophysical Research: Solid Earth 118, 5920–5938. doi:10.1002/2013JB010466.

GFZ Data Services, 1993. GEOFON Data Centre: GEOFON Seismic Network. doi:10.14470/TR560404.

Hayes, G.P., Moore, G.L., Portner, D.E., Hearne, M., Flamme, H., Furtney, M., Smoczyk, G.M., 2018. Slab2, a comprehensive subduction zone geometry model. Science 362, 58–61. doi:10.1126/science.aat4723.

Heuret, A., Lallemand, S., 2005. Plate motions, slab dynamics and back-arc deformation. Physics of the Earth and Planetary Interiors 149, 31–51. doi:10.1016/j.pepi.2004.08.022. thermal Structure and Dynamics of Subduction Zones: Insights from Observations and Modeling.

Institut de physique du globe de Paris (IPGP), École et Observatoire des Sciences de la Terre de Strasbourg (EOST), 1982. Geoscope, french global network of broad band seismic stations. doi:10.18715/GEOSCOPE.G.

Instituto de Geofísica, Universidad Nacional Autónoma de México, México, 2024. SSN: Servicio Sismológico Nacional. doi:10.21766/SSNMX/SN/MX.

Isse, T., Shiobara, H., Montagner, J.P., Sugioka, H., Ito, A., Shito, A., Kanazawa, T., Yoshizawa, K., 2010. Anisotropic structures of the upper mantle beneath the northern Philippine Sea region from Rayleigh and Love wave tomography. Physics of the Earth and Planetary Interiors 183, 33–43. doi:10.1016/j.pepi.2010.04.006.

Karato, S., Jung, H., Katayama, I., Skemer, P., 2008. Geodynamic Significance of Seismic Anisotropy of the Upper Mantle: New Insights from Laboratory Studies. Annual Review of Earth and Planetary Sciences 36, 59–95. doi:10.1146/annurev.earth.36.031207.124120.

Kneller, E., van Keken, P., 2008. Trench-parallel flow and seismic anisotropy in the mariana and andean subduction systems. Nature 450, 1222–1225. doi:10.1038/nature06429.

Kneller, E.A., van Keken, P.E., Karato, S., Park, J., 2005. B-type olivine fabric in the mantle wedge: Insights from high-resolution non-newtonian subduction zone models. Earth and Planetary Science Letters 237, 781–797. doi:10.1016/j.epsl.2005.06.049.

Kreemer, C., Blewitt, G., Klein, E.C., 2014. A geodetic plate motion and Global Strain Rate Model. Geochemistry, Geophysics, Geosystems 15, 3849–3889. doi:10.1002/2014GC005407.

Link, F., Reiss, M.C., Rümpker, G., 2022. An automatized XKS-splitting procedure for large data sets: Extension package for SplitRacer and application to the USArray. Computers & Geosciences 158, 104961. doi:10.1016/j.cageo.2021.104961.

Link, F., Rümpker, G., 2023. Shear-wave splitting reveals layered-anisotropy beneath the european alps in response to mediterranean subduction. Journal of Geophysical Research: Solid Earth 128, e2023JB027192. doi:10.1029/2023JB027192.

Long, M.D., 2013. Constraints on subduction geodynamics from seismic anisotropy. Reviews of Geophysics 51, 76–112. doi:10.1002/rog.20008.

Long, M.D., Becker, T., 2010. Mantle dynamics and seismic anisotropy. Earth and Planetary Science Letters 297, 341–354. doi:10.1016/j.epsl.2010.06.036.

Long, M.D., Silver, P.G., 2008. The subduction zone flow field from seismic anisotropy: A global view. Science 319, 315–318. doi:10.1126/science.1150809.

Long, M.D., Silver, P.G., 2009. Shear Wave Splitting and Mantle Anisotropy: Measurements, Interpretations, and New Directions. Surveys in Geophysics 30, 407–461. doi:10.1007/s10712-009-9075-1.

Long, M.D., van der Hilst, R.D., 2005. Upper mantle anisotropy beneath Japan from shear wave splitting. Physics of the Earth and Planetary Interiors 151, 206–222. doi:10.1016/j.pepi.2005.03.003.

Long, M.D., van der Hilst, R.D., 2006. Shear wave splitting from local events beneath the Ryukyu arc: Trench-parallel anisotropy in the mantle wedge. Physics of the Earth and Planetary Interiors 155, 300–312. doi:10.1016/j.pepi.2006.01.003.

Long, M.D., Wirth, E.A., 2013. Mantle flow in subduction systems: The mantle wedge flow field and implications for wedge processes. Journal of Geophysical Research: Solid Earth 118, 583–606. doi:10.1002/jgrb.50063.

Lynner, C., Long, M.D., 2014. Lowermost mantle anisotropy and deformation along the boundary of the African LLSVP. Geophysical Research Letters , 3447–3454doi:10.1002/2014GL059875.

Lynner, C., Long, M.D., 2015. Heterogeneous seismic anisotropy in the transition zone and uppermost lower mantle: evidence from South America, Izu-Bonin and Japan. Geophysical Journal International 201, 1545–1552. doi:10.1093/gji/ggv099.

Müller, D., Zahirovic, S., Williams, S., Cannon, J., Seton, M., Bower, D., Tetley, M., Heine, C., Le Breton, E., Liu, S., Russell, S., Yang, T., Leonard, J., Gurnis, M., 2019. A Global Plate Model Including Lithospheric Deformation Along Major Rifts and Orogens Since the Triassic. Tectonics 38. doi:10.1029/2018TC005462.

Paczkowski, K., Montési, L.G.J., Long, M.D., Thissen, C.J., 2014a. Three-dimensional flow in the subslab mantle. Geochemistry, Geophysics, Geosystems 15, 3989–4008. doi:10.1002/2014GC005441.

Paczkowski, K., Thissen, C.J., Long, M.D., Montési, L.G.J., 2014b. Deflection of mantle flow beneath subducting slabs and the origin of subslab anisotropy. Geophysical Research Letters 41, 6734–6742. doi:10.1002/2014GL060914.

Pozgay, S.H., Wiens, D.A., Conder, J.A., Shiobara, H., Sugioka, H., 2007. Complex mantle flow in the mariana subduction system: evidence from shear wave splitting. Geophysical Journal International 170, 371–386. doi:10.1111/j.1365-246X.2007.03433.x.

Reiss, M., Rümpker, G., 2017. SplitRacer: MATLAB Code and GUI for Semiautomated Analysis and Interpretation of Teleseismic Shear-Wave Splitting. Seismological Research Letters 88, 392–409. doi:10.1785/0220160191.

RESIF, 1995. RESIF-RLBP French Broad-band network, RESIF-RAP strong motion network and other seismic stations in metropolitan France. doi:10.15778/RESIF.FR.

Russo, R., Gallego, A., Comte, D., Mocanu, V., Murdie, R., VanDecar, J., 2010. Source-side shear wave splitting and upper mantle flow in the Chile Ridge subduction Region. Geology 38, 707–710. doi:10.1130/G30920.1.

Savage, M.K., 1999. Seismic anisotropy and mantle deformation: What have we learned from shear wave splitting? Reviews of Geophysics 37, 65 – 106. doi:10.1016/10.1029/98RG02075.

Schaeffer, A., Lebedev, S., Becker, T., 2016. Azimuthal seismic anisotropy in the Earth's upper mantle and the thickness of tectonic plates. Geophysical Journal International 207, 901–933. doi:10.1093/gji/ggw309.

Sieminski, A., Paulssen, H., Trampert, J., Tromp, J., 2008. Finite-frequency sks splitting: Measurement and sensitivity kernels. Bulletin of the Seismological Society of America 98, 1797–1810. doi:10.1785/0120070297.

Silver, P.G., Chan, W.W., 1991. Shear wave splitting and subcontinental mantle deformation. Journal of Geophysical Research: Solid Earth 96, 16429–16454. doi:10.1029/91JB00899.

Song, T.R.A., Kawakatsu, H., 2012. Subduction of oceanic asthenosphere: Evidence from sub-slab seismic anisotropy. Geophysical Research Letters 39. doi:10.1029/2012GL052639.

Steinberger, B., Becker, T.W., 2018. A comparison of lithospheric thickness models. Tectonophysics 746, 325–338. doi:https://doi.org/10.1016/j.tecto.2016.08.001.

Su, L., Park, J., 1994. Anisotropy and the splitting of PS waves. Physics of the Earth and Planetary Interiors 86, 263–276. doi:10.1016/0031-9201(94)90125-2.

UC Berkeley Seismological Laboratory, 2014. Northern California Earthquake Data Center. doi:10.7932/NCEDC.

Vinnik, L., Farra, V., Romanowicz, B., 1989. Azimuthal anisotropy in the earth from observations of SKS at GEOSCOPE and NARS broadband stations. Bulletin - Seismological Society of America 79, 1542–1558. doi:10.1785/BSSA0790051542.

Walsh, E., Arnold, R., Savage, M.K., 2013. Silver and Chan revisited. Journal of Geophysical Research: Solid Earth 118, 5500–5515. doi:10.1002/jgrb.50386.

Wang, L., He, X., 2020. Seismic Anisotropy in the Java-Banda and Philippine Subduction Zones and its Implications for the Mantle Flow System Beneath the Sunda Plate. Geochemistry, Geophysics, Geosystems 21, e2019GC008658. doi:10.1029/2019GC008658.

Wessel, P., Smith, W.H.F., 1998. New, improved version of generic mapping tools released. Eos, Transactions American Geophysical Union 79, 579–579. doi:10.1029/98EO00426.

Wirth, E., Long, M.D., 2010. Frequency-dependent shear wave splitting beneath the japan and izu-bonin subduction zones. Physics of the Earth and Planetary Interiors 181, 141–154. URL: https://doi.org/10.1016/j.pepi.2010.05.006.

Wolf, J., Becker, T.W., Garnero, E., Liu, K.H., West, J.D., 2025. Comprehensive global dataset of uniformly processed shear-wave splitting measurements. Geophysical Journal International doi:10.1093/gji/ggaf076.

Wolf, J., Frost, D.A., Brewster, A., Long, M.D., Garnero, E., West, J.D., 2024a. Widespread D″ anisotropy beneath North America and the northeastern Pacific and implications for upper mantle anisotropy measurements. Journal of Geophysical Research: Solid Earth doi:10.1029/2024JB029516.

Wolf, J., Li, M., Haws, A.A., Long, M.D., 2024b. Strong seismic anisotropy due to upwelling flow at the root of the Yellowstone mantle plume. Geology doi:10.1130/G51919.1.

Wolf, J., Long, M.D., 2023. Upper Mantle Anisotropy and Flow Beneath the Pacific Ocean Revealed by Differential PS-SKS Splitting. Geophysical Research Letters 50, e2023GL104402. doi:10.1029/2023GL104402.

Wolf, J., Long, M.D., Frost, D.A., 2024c. Ultralow velocity zone and deep mantle flow beneath the Himalayas linked to subducted slab. Nature Geoscience , 1–7doi:10.1038/s41561-024-01386-5.

Wolf, J., Long, M.D., Frost, D.A., Nissen-Meyer, T., 2024d. The expression of mantle seismic anisotropy in the global seismic wavefield. Geophysical Journal International 238, 346–363. doi:10.1093/gji/ggae164.

Yeh, Y.L., Kao, H., Wen, S., Chang, W.Y., Chen, C.H., 2013. Surface wave tomography and azimuthal anisotropy of the Philippine Sea Plate. Tectonophysics 592, 94–112. doi:j.tecto.2013.02.005.